Acta Pharmaceutica Sinica B 2025;15(4):2237−2252

Chinese Pharmaceutical Association
Institute of Materia Medica, Chinese Academy of Medical Sciences

Acta Pharmaceutica Sinica B

www.elsevier.com/locate/apsb
www.sciencedirect.com

ORIGINAL ARTICLE

siRNA micelleplexes-mediated glutamine metabolism re-engineering for vascular normalization-boosted photo-immunotherapy

Yunfei Yi[a,b,c,†], Zhangwen Peng[b,†], Yuanqi Liu[b], Huisong Hao[b], Liu Yu[a], Simin Wen[b], Shengjie Sun[b], Jianlin Shi[c,*], Meiying Wu[b,*], Lin Mei[a,b,*]

[a]*State Key Laboratory of Advanced Medical Materials and Devices, Tianjin Key Laboratory of Biomedical Materials, Key Laboratory of Biomaterials and Nanotechnology for Cancer Immunotherapy, Institute of Biomedical Engineering, Chinese Academy of Medical Sciences and Peking Union Medical College, Tianjin 300192, China*
[b]*School of Pharmaceutical Sciences (Shenzhen), Shenzhen Campus of Sun Yat-sen University, Shenzhen 518107, China*
[c]*Shanghai Institute of Ceramics, Chinese Academy of Sciences, Research Unit of Nanocatalytic Medicine in Specific Therapy for Serious Disease, Chinese Academy of Medical Sciences, Shanghai 200050, China*

Received 12 August 2024; received in revised form 15 November 2024; accepted 25 December 2024

KEY WORDS

Glutaminolysis inhibition;
Tumor vascular normalization;
TAM repolarization;
Photo-immunotherapy;
Immunogenic cell death;
Immunosuppressive tumor microenvironment;
Glutaminase 1;
Photodynamic therapy

Abstract Among tumor microenvironment (TME), the entire metabolic characteristics of tumor-resident cells are reprogrammed to benefit the expansion of tumor cells, which count on glutamine in large part to fuel the tricarboxylic acid cycle for energy generation and anabolic metabolism support. Endothelial cells that are abducted by tumor cells to form a pathological tumor vascular network for constructing the hypoxic immunosuppressive TME, also rely on glutaminolysis as the "engine" of angiogenesis. Additionally, the glutamine metabolic preference benefits the polarization of TAMs towards pro-tumoral M2 phenotype as well. Herein, we developed a type of siRNA micelleplexes (MH@siGLS1) to reverse immunosuppressive TME by targeting glutaminolysis within tumor-resident cells for tumor vasculature normalization- and TAMs repolarization-enhanced photo-immunotherapy. Tumor cell starvation and antioxidant system destruction achieved by MH@siGLS1-mediated glutaminolysis inhibition could promote photodynamic therapy efficacy, which was available to trigger immunogenic

*Corresponding authors.
E-mail addresses: jlshi@mail.sic.ac.cn (Jianlin Shi), wumy53@mail.sysu.edu.cn (Meiying Wu), meilin@bme.pumc.edu.cn (Lin Mei).
[†]These authors made equal contributions to this work.
Peer review under the responsibility of Chinese Pharmaceutical Association and Institute of Materia Medica, Chinese Academy of Medical Sciences.

https://doi.org/10.1016/j.apsb.2025.02.020

cell death for adaptive antitumor immune responses. Meanwhile, glutaminolysis inhibition of tumor endothelial cells and TAMs could realize tumor vascular normalization and TAMs repolarization for antitumor immunity amplification. This study provides a unique perspective on cancer treatments by focusing on the interrelations of metabolic characteristics and the biofunctions of various cell types within TME.

1. Introduction

Cancer cells are adept at using distinct metabolic pathways to meet the prodigious requirements of energy and anabolism for malignant growth, among which Warburg metabolism was preferred to rapidly catabolize glucose for quick energy acquisition and production of intermediate metabolites[1,2]. However, the enormous glucose demand in the tumor microenvironment (TME) does not count on tumor cells merely, by contrast, the tumor-resident cell population in TME which consumes the most glucose belongs to myeloid cells, followed by T cells and tumor cells based on their selective nutrient partitioning[3]. It is worth noting that tumor cells exhibit the highest uptake of glutamine (Gln)[3], which plays an essential role in fueling the tricarboxylic acid (TCA) cycle by being converted to α-ketoglutarate (α-KG) *via* glutaminolysis for amino acid and fatty acid synthesis, as well as *de novo* synthesis of purines and pyrimidines since most glucose-derived carbon is excreted as lactate rather than entering the TCA cycle[4]. On that account, it is an attainable approach to terminate the survival of tumor cells by inhibiting glutaminolysis.

Glutaminolysis (also known as Gln metabolism) within tumor cells is initiated from the conversion of cell transported-Gln to glutamate (Glu) *via* mitochondrial glutaminase (GLS1)[5]. Aside from supporting energy production and biomass synthesis for rapid tumor growth and proliferation, glutaminolysis also engages in the synthesis process of glutathione (GSH) by directly and indirectly influencing the three amino acid components of GSH, a tripeptide (Glu-Cys-Gly) that could neutralize reactive oxygen species (ROS), to maintain the cellular redox equilibrium state of tumor cells[4,6,7]. As another type of essential member of the antioxidant system, nicotinamide adenine dinucleotide phosphate (NADPH) is closely associated with glutaminolysis as well through being converted from TCA-derived cytoplasm malate[4,8,9]. In order to resist oxidative stress damage, tumor cells are usually proficient in evolving formidable antioxidant systems by upregulating GSH and NADPH, etc., which significantly impair the therapeutic effectiveness of external oxidative treatments such as photodynamic therapy (PDT) and chemodynamic therapy (CDT)[10,11].

In actual fact, the malignant expansion of tumors is not only related to the dysfunction of tumor cells themselves but also involves the complicated interrelations of the other components in TME[12,13], among which the pathological tumor vasculature is a nonnegligible backstage driving force[14-16]. The sharp proliferation of solid tumors leads to a dramatic increase in the demand for nutrients, so angiogenesis is rapidly initiated under the regulation of various angiogenic signals to acquire sufficient blood supply[17-19]. Unlike healthy orderly vessels, the tortuous, saccular, and leaky tumor vessels characterized by loosed connected endothelial cells (ECs) and detached pericytes tend to establish a chaotic tumor vascular network, which promotes the formation of the immunosuppressive TME featured with hypoxia, acidity and high interstitial pressure[20-22]. Such an atrocious TME not only influences the therapeutic efficiency of oxygen-dependent drugs but also hampers the bioactivity of immune effector cells[23,24]. Furthermore, it has been reported that the expressions of cell adhesion molecules are downregulated in the tumor-associated ECs, resulting in endothelial anergy and inhibiting the trafficking of immune effector cells into the tumor bed, thus further hampering antitumor immunity[24,25].

In the past traditional therapies against tumor angiogenesis, angiogenic signals and their membrane receptors, as well as downstream signaling cascades have been kept in a central position for drug target selections[26,27]. The star angiogenic growth factor, vascular endothelial growth factor (VEGF), which plays a key role in angiogenesis, is the best illustration[28,29]. Despite there being stacks of clinically approved anti-angiogenic drugs targeting angiogenic factors and receptors, insufficient therapeutic efficiency still appears due to drug resistance, systemic toxicity, and most importantly, once one growth factor (receptor) is blocked, it may compensatively promote the upregulation of others[26,30,31]. Taking angiogenesis as a process of starting a car, angiogenic factors and the downstream signals function like drivers, while the endothelial cell metabolism acts as the engine. Instead of removing a driver that could be replaced with a similar one, jamming the engine might be a more promising strategy to block tumor angiogenesis[26,32]. Even exposed to high blood-oxygen concentrations in healthy conditions, ECs prefer glycolytic metabolism rather than oxidative glucose metabolism for certain advantages[33], for example, to protect themselves from ROS production, support energy generation for vascularization in avascular hypoxic regions, and save oxygen for transfer to perivascular cells[26,34]. Similar to tumor cells, in order to supply enough energy for angiogenesis, the compensatory Gln metabolism (glutaminolysis) is of great importance in fueling the TCA cycle *via* replenishing carbon and nitrogen flux to support biomass synthesis for ECs proliferation and migration[26,35].

As the main infiltrated immune cells in TME, tumor-associated macrophages (TAMs) could differentiate into anti-tumoral M1 phenotype and pro-tumoral M2 phenotype along with metabolic switching. Gln deprivation or glutaminolysis suppression could hinder M2 polarization but not M1 polarization by inhibiting UDP-GlcNAc biosynthesis and N-glycosylation of certain typical M2 macrophage proteins such as CD206[36]. Besides, hypoxia could also promote M2 polarization[37]. As a considerable major immunosuppressive cell population in TME which could secrete immunosuppressive cytokines (such as IL-6, IL-10 and TGF-β) and angiogenic factors (such as VEGF and PDGF), M2 macrophages are able to directly promote the growth of tumor cells, hamper the bioactivity of immune effector T cells, recruit immunosuppressive regulatory T (Treg) cells, and participate in

angiogenesis, thus further promoting tumor escape and invasion[38]. Blocking glutaminolysis could interrupt the cellular metabolism within the whole TME, including immune effector T cells, which are not metabolically disabled but unexpectedly enhanced to be a long-lived, highly activated phenotype by adopting acetate as a carbon source for the TCA cycle[39]. As such, glutaminolysis is regarded as a metabolic checkpoint for antitumor immunotherapy, and blocking glutaminolysis possesses the potential to restore the effectiveness of immune effector cells[39].

Herein, we constructed a type of siRNA micelleplexes to achieve immunosuppressive TME reversion by targeting glutaminolysis for synergistic antitumor photo-immunotherapy. An amphiphilic cationic triblock copolymer consisting of monomethoxy (polyethylene glycol)-poly ($_{D,L}$-lactide-*co*-glycolide)-poly ($_{L}$-lysine) (mPEG-PLGA-PLL) was synthesized according to the reported method[40]. The obtained triblock copolymer mPEG-PLGA-PLL was assembled with the hydrophobic photosensitizer hematoporphyrin monomethyl ether (HMME) through hydrophobic interaction to acquire MH micelleplexes, which could further bound with small interfering RNA (siRNA) against GLS1 *via* electrostatic adsorption to the cationic segment PLL (designated as MH@siGLS1; Fig. 1A). Such micelleplexes could re-engineer the metabolic characteristics of various cell types within TME including tumor cells, ECs, TAMs and T cells, thus realizing vascular-normalization-boosted immune cells infiltration and hypoxia alleviation, which in turn proceeded the repolarization speed of TAMs from M2 to M1 phenotype, and amplified PDT-mediated immunogenic cell death (ICD), enhancing antitumor efficiency in synergy with tumor cell starvation effect (Fig. 1B). To sum up, this work provides a new perspective to improve antitumor photo-immunotherapy by regulating the metabolism characteristic of tumor-resident cells for TME normalization. The constructed MH@siGLS1 could exert superb immune responses to inhibit tumor growth by reversing immunosuppressive TME through tumor vascular normalization and TAMs repolarization, significantly releasing the antitumor activity of immune effector cells.

2. Materials and methods

2.1. Reagents

Hematoporphyrin monomethyl ether (HMME) was obtained from Shanghai D&B Biotechnology Co., Ltd. Sulfoxide (DMSO) was provided by Aladdin. Sodium phosphotungstate was purchased from G-CLONE. Pyrene and 2′,7′-dichlorofluorescein diacetate (DCFH-DA) were purchased from Sigma−Aldrich. siGLS1, negative control siRNA (siNC), and carboxyfluorescein (FAM)-labeled siRNA (siFAM) were purchased from Guangzhou Ruibo Bio-Technology. ThiolTracker™ Violet and Singlet Oxygen Sensor Green were obtained from ThermoFisher Scientific. The Enhanced ATP Assay Kit, GelRed, and the Enhanced BCA Protein Assay Kit were purchased from Beyotime Biotechnology. Mouse antibodies against α-SMA, CRT, HMGB1, HIF-1α, and VEGF were purchased from Abcam. Mouse antibody against CD31 was provided by Cell Signaling Technology. Mouse antibodies against GLS1 and β-actin were obtained from Beijing Bioss Biotechnology Co., Ltd. TNF-α, IFN-γ, IL-2, and IL-10 enzyme-linked immunosorbent assay (ELISA) kits were purchased from Beijing Solarbio Science & Technology Co., Ltd. The cationic triblock copolymer mPEG-PLGA-PLL was synthesized by Hangzhou Xinqiao Biotechnology Co., Ltd.

2.2. Animals

Female C57BL/6 mice (4−5 weeks old) were obtained from Guangdong Medical Laboratory Animal Center (Guangzhou, China). All experimental procedures were executed according to the protocols approved by Animal Ethical and Welfare Committee (AEWC) (approval number: IRM-DWLL-2022024). Animals were allowed to eat freely and randomized before the experiment.

2.3. Preparation of MH@siGLS1 micelleplexes

To construct MH@siGLS1 micelleplexes, the cationic triblock copolymer mPEG-PLGA-PLL and HMME were respectively dissolved in DMSO, and then mixed at a weight ratio of 4:1. The above mixture was then stepwise added into DNase/RNase-free water under ultrasonication (120 W) for 20 min and incubated at room temperature for 1 h to allow self-assembly. The obtained solution was then transferred into an ultrafiltration centrifugal tube (15 mL, MWCO 100K) and centrifuged at 5000 rpm for 10 min to remove the organic solvent DMSO. The concentrated product was dispersed in DNase/RNase-free water to obtain MH micelleplexes. After further being mixed with siGLS1 (dissolved in DNase/RNase-free water) at room temperature for 30 min, MH@siGLS1 micelleplexes were finally constructed.

2.4. Critical micelle concentration of MH@siGLS1 micelleplexes

To determine the critical micelle concentration (CMC), a series of MH@siGLS1 micelleplexes aqueous solutions with different molar concentrations (0.01−200 μmol/L) were prepared first and then incubated with the fluorescence probe pyrene (10^{-6} mol/L) at 37 °C for 2 h. The above samples were detected using an LS 55 fluorescence spectrophotometer at the excitation wavelength of 334 nm, and their emission fluorescence spectrum from 300 to 550 nm was recorded. The CMC value was equal to the emission fluorescence intensity ratio of 384 and 373 nm (I_{384}/I_{373}).

2.5. In vitro $^1O_2$ detection of MH@siGLS1 micelleplexes

Fluorescence probe SOSG was adopted to detect the singlet oxygen production. Specifically, 2.5 μmol/L SOSG was mixed with MH@siGLS1 micelleplexes aqueous solution (HMME: 5 μg/mL), which further received irradiation under 658 nm laser (100 mW/cm^2) for 10 min or stayed in dark. The emission fluorescence intensity of oxidized SOSG at 525 nm in each sample was recorded by an LS 55 fluorescence spectrophotometer (excitation wavelength: 488 nm) at different time points. Solvent DNase/RNase-free water was set as negative control.

2.6. Agarose gel retardation assay

The condensing capability of MH micelleplexes for siGLS1 was first explored *via* agarose gel retardation assay. siGLS1 (0.27 μg) was complexed with MH micelleplexes at different *N*/*P* ratios for 30 min at room temperature. After adding RNA loading buffer, the obtained mixtures (10 μL) were loaded onto 1% agarose gel containing GelRed in the solvent environment of Tris-acetate EDTA (TAE). Then agarose gel electrophoresis was conducted at 80 V for 30 min and RNA bands were finally visualized using the BioRad imaging system (USA).

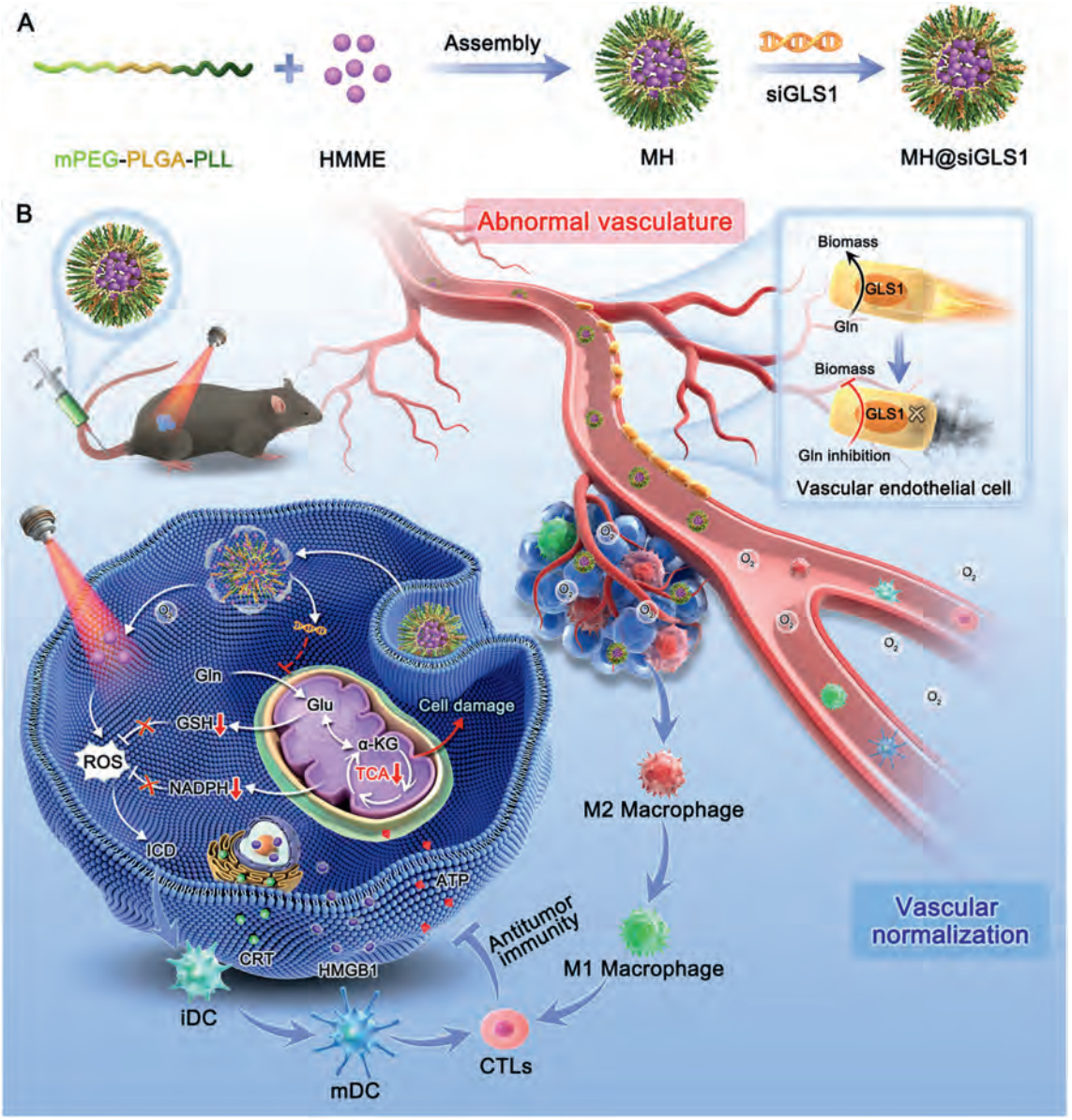

Figure 1 Schematic illustration of MH@siGLS1 micelleplexes for vascular normalization-boosted photo-immunotherapy. (A) Composition and preparation of MH@siGLS1 micelleplexes. (B) Antitumor mechanism of MH@siGLS1-mediated synergistic vascular normalization for enhanced photo-immunotherapy.

2.7. *In vitro siRNA transfection*

To detect the siRNA transfection efficacy, MC38 cells were seeded in confocal dishes (3×10^5 cells per dish) and cultured for 24 h at 37 °C under 5% CO_2 atmosphere. The adherent cells were then incubated with free siFAM, Lipofectamine 2000@siFAM, or MH@siFAM (HMME: 10 μg/mL; siFAM: 2 μg/mL) for 6 h. After washed with PBS, the cells were fixed with paraformaldehyde (4%) solution, and the nuclei were stained with 4′,6-diamidino-2-phenylindole (DAPI). The fluorescence signals of DAPI and siFAM were observed using CLSM.

2.8. *Cellular uptake*

For cellular uptake, MC38 cells were seeded in confocal dishes (3×10^5 cells per dish) and cultured for 24 h at 37 °C under 5% CO_2 atmosphere. Subsequently, the cells were incubated with free HMME or MH@siGLS1 at the HMME concentration of 10 μg/mL for different times (0.5, 2, 4, and 6 h). After washed with PBS, the cells were fixed with paraformaldehyde (4%) solution, and the nuclei were stained with DAPI. The fluorescence signals of DAPI and HMME were observed using CLSM.

2.9. *In vitro GSH depletion*

For intracellular GSH depletion, MC38 cells were seeded in confocal dishes (3×10^5 cells per dish) and cultured for 24 h at 37 °C under 5% CO_2 atmosphere. Afterward, the cells were incubated with MH@siNC or MH@siGLS1 at an equivalent HMME concentration (10 μg/mL). The untreated MC38 cells were set as the control group. After incubation for 12 h, the cells were irradiated with a 658 nm laser for 5 min (100 mW/cm^2) or

kept in the dark. Subsequently, the cells were washed with PBS and further incubated with DMEM containing the fluorescence probe ThiolTracker Violet (20 μmol/L) for 30 min. The fluorescence signals of DAPI and ThiolTracker Violet were observed using CLSM.

2.10. *In vitro NADPH depletion*

For intracellular NADPH depletion, MC38 cells were seeded into 6-well plates (3×10^5 cells per well) and cultured for 24 h at 37 °C under 5% CO_2 atmosphere. Afterward, the cells were incubated with MH@siNC or MH@siGLS1 at an equivalent HMME concentration (10 μg/mL). The untreated MC38 cells were set as the control group. After incubation for 12 h, the cells were irradiated with a 658 nm laser for 5 min (100 mW/cm^2) or kept in the dark. Subsequently, the cells were collected by trypsin and the intracellular NADPH content was examined according to the NADPH Determination Kit.

2.11. *In vitro ROS generation*

Intracellular ROS generation was analyzed using CLSM and flow cytometry by adopting DCFH-DA as the fluorescence probe. For CLSM examination, MC38 cells were seeded in confocal dishes (3×10^5 cells per dish) and cultured for 24 h at 37 °C under 5% CO_2 atmosphere. Afterward, the cells were incubated with MH@siNC or MH@siGLS1 at an equivalent HMME concentration (10 μg/mL). The untreated MC38 cells were set as the control group. After incubation for 12 h, the cells were further incubated with PBS containing DCFH-DA (20 mmol/L) for 20 min, followed by irradiation with a 658 nm laser for 5 min (100 mW/cm^2) or kept in the dark. The cells were next stained with DAPI and observed using CLSM. For flow cytometry, MC38 cells were seeded into 6-well plates (3×10^5 cells per well) and cultured for 24 h. The next procedures stayed the same as those in the above process until the irradiation step. After laser irradiation, the cells were collected by trypsin and examined using flow cytometry.

2.12. *GLS1 silencing*

The silencing effect of GLS1 was examined using western blotting. MC38 cells were seeded into 6-well plates (4×10^5 cells per well) and cultured for 24 h at 37 °C under 5% CO_2 atmosphere. Afterward, the cells were incubated with MH@siNC or MH@siGLS1 (2 μg siRNA). The untreated MC38 cells were set as the control group. After incubation for 72 h, the cells were collected by trypsin for GLS1 expression analysis using Western blotting.

2.13. *In vitro cytotoxicity*

MC38 cells were seeded in 96-well plates (8×10^3 cells per well) and cultured for 24 h at 37 °C under 5% CO_2 atmosphere. Afterward, the cells were incubated with MH@siNC or MH@siGLS1 (HMME: 10 μg/mL, siRNA: 2 μg/mL). The untreated MC38 cells were set as the control group. After incubation for 12 h, the cells were irradiated with a 658 nm laser for 3 min (100 mW/cm^2) or kept in the dark and then further incubated for 36 h. The cell viability was assessed using the standard CCK-8 method.

2.14. *Tube formation assay*

The tube formation assay was performed to assess the inhibitory efficiency of MH@siGLS1 on mice aortic endothelial cells (MAEC) vascularization. Briefly, MAEC cells were seeded into 6-well plates (3×10^5 cells per well) and cultured for 24 h at 37 °C under 5% CO_2 atmosphere. Afterward, the cells were incubated with MH@siNC or MH@siGLS1 (HMME: 10 μg/mL, siRNA: 2 μg/mL). The untreated MAEC cells were set as the control group. After incubation for 6 h, the cells were collected by trypsin and resuspended in DMEM containing 50 ng/mL VEGF. The resuspended cells were further seeded into a Matrigel-coated 96-well plate (2.5×10^4 cells per well). After incubation for 4 h, the tubule formation was observed by an inverted microscope, and the tubule length and branch points of the tubules in different groups were calculated using ImageJ software.

2.15. *Transwell cell migration assay*

The transwell cell migration assay was performed to assess the inhibitory efficiency of MH@siGLS1 on MAEC vascularization. Briefly, MAEC cells (1×10^5 per well) in 100 μL pure DMEM medium containing MH@siNC or MH@siGLS1 (HMME: 5 μg/mL, siRNA: 1 μg/mL) were seeded into the upper chambers, and complete DMEM medium was added into the lower chambers. 24 h later, the MAEC cells that migrated through the transwell membrane were fixed with paraformaldehyde, stained with crystal violet, and observed by an inverted microscope. The migration rates in different groups were calculated using ImageJ software.

2.16. *In vitro examination of ICD biomarkers*

The surface-exposed CRT and the nucleus-located HMGB1 were detected using CLSM and flow cytometry. For CLSM analysis, MC38 cells were seeded in confocal dishes (3×10^5 cells per dish) and cultured for 24 h at 37 °C under 5% CO_2 atmosphere. The cells were incubated with MH@siNC or MH@siGLS1 (HMME: 10 μg/mL, siRNA: 2 μg/mL). The untreated MC38 cells were set as the control group. After incubation for 12 h, the cells were irradiated with a 658 nm laser for 5 min (100 mW/cm^2) or kept in the dark. Afterward, the cells were stained with anti-CRT (or anti-HMGB1) antibody and DAPI for observation by CLSM. For flow cytometry analysis, MC38 cells were seeded into 6-well plates (3×10^5 cells per well) and cultured for 24 h at 37 °C under 5% CO_2 atmosphere. The subsequent procedures stayed the same as the above procedures until the irradiation step. After laser irradiation, the cells were collected by trypsin, stained with anti-CRT (or anti-HMGB1) antibody, and examined using flow cytometry. For ATP detection, after laser irradiation, the cells in 6-well plates were collected by trypsin for further analysis using the Chemiluminescence ATP Determination Kit.

2.17. *In vitro induction of DC maturation*

Bone marrow cells were collected from 6-week-old C57BL/6 mice. The obtained cells were seeded into 24-well plates (10^5 cells per well) and cultured with complete RPMI 1640 medium containing granulocyte-macrophage colony-stimulating factor (GM-CSF, 20 ng/mL) and interleukin-4 (IL-4, 20 ng/mL) to differentiate into immature DCs. On Day 6, the obtained immature DCs were co-incubated with MC38 cells that had been pretreated

with LPS, MH@siNC, MH@siGLS1, MH@siNC + L or MH@siGLS1+L (HMME: 10 μg/mL, siRNA: 2 μg/mL. The untreated MC 38 cells were set as control). 36 h later, DCs were collected and stained with antibodies (anti-CD11c-APC, anti-CD80-PC5.5, and anti-CD86-FITC), and then examined using flow cytometry. APC, allophycocyanin; PC5.5, PerCP-Cyanine5.5; FITC, fluorescein isothiocyanate.

2.18. *In vitro macrophage repolarization*

RAW 264.7 cells were seeded into 6-well plates (5.5×10^5 cells per well) and incubated for 24 h at 37 °C under 5% CO_2 atmosphere. Afterward, the old medium was replaced with new DMEM containing IL-4 (40 ng/mL) to induce polarization of RAW 264.7 cells towards M2 phenotype after incubation for 24 h. The obtained cells were subsequently incubated with MH@siNC or MH@siGLS1 (HMME: 10 μg/mL, siRNA: 2 μg/mL) for another 12 h. Then the cells were irradiated with a 658 nm laser for 5 min (100 mW/cm^2) or kept in the dark. The cells were collected by trypsin and stained with antibodies (anti-F4/80-APC, anti-CD11b-PE/Cyanine7 and anti-CD206-FITC for M2 macrophage detection, and anti-F4/80-APC, anti-CD11b-PE/Cyanine7 and anti-CD86-FITC for M1 macrophage detection). The macrophage repolarization was examined using flow cytometry.

2.19. *In vivo biodistribution*

The *in vivo* biodistribution characteristic of MH@siGLS1 and free HMME in MC38 tumor-bearing C57BL/6 mice was assessed by intravenously injecting MH@siGLS1 or free HMME (HMME: 2.5 mg/kg) and imaging using the *In Vivo* Imaging System (IVIS) Lumina XR (PerkinElmer, Inc., Waltham, MA, UK) (Ex/Em = 620/650 nm) at different time points (0, 2, 4, 8, 12, 24, 36 and 48 h). After 48 h, the tumors and major organs (heart, liver, spleen, lung, and kidney) were harvested for *ex vivo* fluorescence imaging.

2.20. *In vivo antitumor efficacy*

The inhibition of tumor growth was assessed in a unilateral tumor model. Briefly, MC38 cells (3×10^6) were subcutaneously injected into the right flank of C57BL/6 mice (4−5 weeks). When the tumor volumes reached 100 mm^3, the tumor-bearing mice were randomly divided into 6 groups ($n = 5$ per group) and intravenously injected with PBS, MH@siNC, and MH@siGLS1 respectively (HMME: 5 mg/kg; siRNA: 1 mg/kg). Three irradiated groups (Control + L, MH@siNC + L, and MH@siGLS1+L) received laser irradiation (658 nm, 300 mW/cm^2, 5 min) 24 h post-injection. The treatments were carried out three times every two days, and the tumor volumes and body weights were recorded every two days. The tumor volumes were calculated based on Eq. (1):

$$\text{Tumor volume} = 0.5 \times (\text{Tumor length}) \times (\text{Tumor width})^2 \quad (1)$$

The mice were sacrificed on Day 14, and the tumors and major organs (heart, liver, spleen, lung, and kidney) were collected for tumor photographing, weight measuring, H&E staining, TUNEL staining, and immunostaining.

2.21. *In vivo immune response analysis*

The abscopal effect and *in vivo* immune responses were assessed in the bilateral MC38 tumor model. Briefly, MC38 cells (3×10^6) were subcutaneously injected into the right flank of C57BL/6 mice (4−5 weeks; designated as the primary tumor). Nine days later, MC38 cells (5×10^5) were subcutaneously injected into the left flank of the tumor-bearing C57BL/6 mice (designated as the abscopal tumor). When the primary tumor volumes reached 110 mm^3, the mice were randomly divided into 6 groups ($n = 5$ per group) and intravenously injected with PBS, MH@siNC, and MH@siGLS1 respectively (HMME: 5 mg/kg; siRNA: 1 mg/kg). Three irradiated groups (Control + L, MH@siNC + L, and MH@siGLS1+L) received laser irradiation (658 nm, 300 mW/cm^2, 5 min) 24 h post-injection. The treatments were carried out five times every three days, and the tumor volumes and body weights were recorded every two days. The tumor volumes were calculated based on Eq. (2):

$$\text{Tumor volume} = 0.5 \times (\text{Tumor length}) \times (\text{Tumor width})^2 \quad (2)$$

The mice were sacrificed on Day 14, and the tumors and TDLNs were collected. Half primary tumor tissues were utilized for flow cytometry examination of $CD4^+$ T cells (anti-CD3-APC and anti-CD4-FITC), $CD8^+$ T cells (anti-CD3-APC and anti-CD8a-PE/Cyanine7), Treg cells (anti-CD3-APC, anti-CD4-Pacific Blue and anti-Foxp3-PE), M2 macrophages (anti-F4/80-APC, anti-CD11b-PE/Cyanine7 and anti-CD206-FITC), and M1 macrophages (anti-F4/80-APC, anti-CD11b-PE/Cyanine7 and anti-CD86-FITC). The other half of the tumor tissues were utilized for ELISA analysis of TNF-α, IFN-γ, IL-2, and IL-10. The TDLNs were utilized for flow cytometry examination of mature DCs (anti-CD11c-APC, anti-CD80-PC5.5, and anti-CD86-FITC).

2.22. *Statistical analysis*

The results were expressed as mean ± standard deviation (SD). A two-tailed unpaired Student's *t*-test and one-way ANOVA were used to analyze the statistical differences. Significant values were implied as below: $^*P < 0.05$, $^{**}P < 0.01$, $^{***}P < 0.001$, ns, not significant.

3. Results and discussion

3.1. *Preparation of MH@siGLS1 micelleplexes*

The cationic triblock copolymer mPEG-PLGA-PLL was synthesized (Supporting Information Fig. S1) and characterized by Fourier Transform Infrared Spectroscopy (FTIR) (Fig. 2A) and ^{1}H Nuclear Magnetic Resonance (^{1}H NMR) (Supporting Information Fig. S2) to verify the chemical structure. The synthesized mPEG-PLGA-PLL was able to self-assemble into blank micelles in an aqueous solution (designated as M) at room temperature (Supporting Information Fig. S3). The hydrophobic core formed by the polymer PLGA block of M could encapsulate HMME (designated as MH) and exhibited well-defined uniform spherical morphology according to the transmission electron microscopy (TEM) image (Fig. 2B). The cationic PLL block of MH was able to further integrate electronegative siGLS1 *via* electrostatic force, and larger sizes of the obtained micelleplexes (designated as MH@siGLS1) (Fig. 2C) than MH were observed with an average hydrodynamic

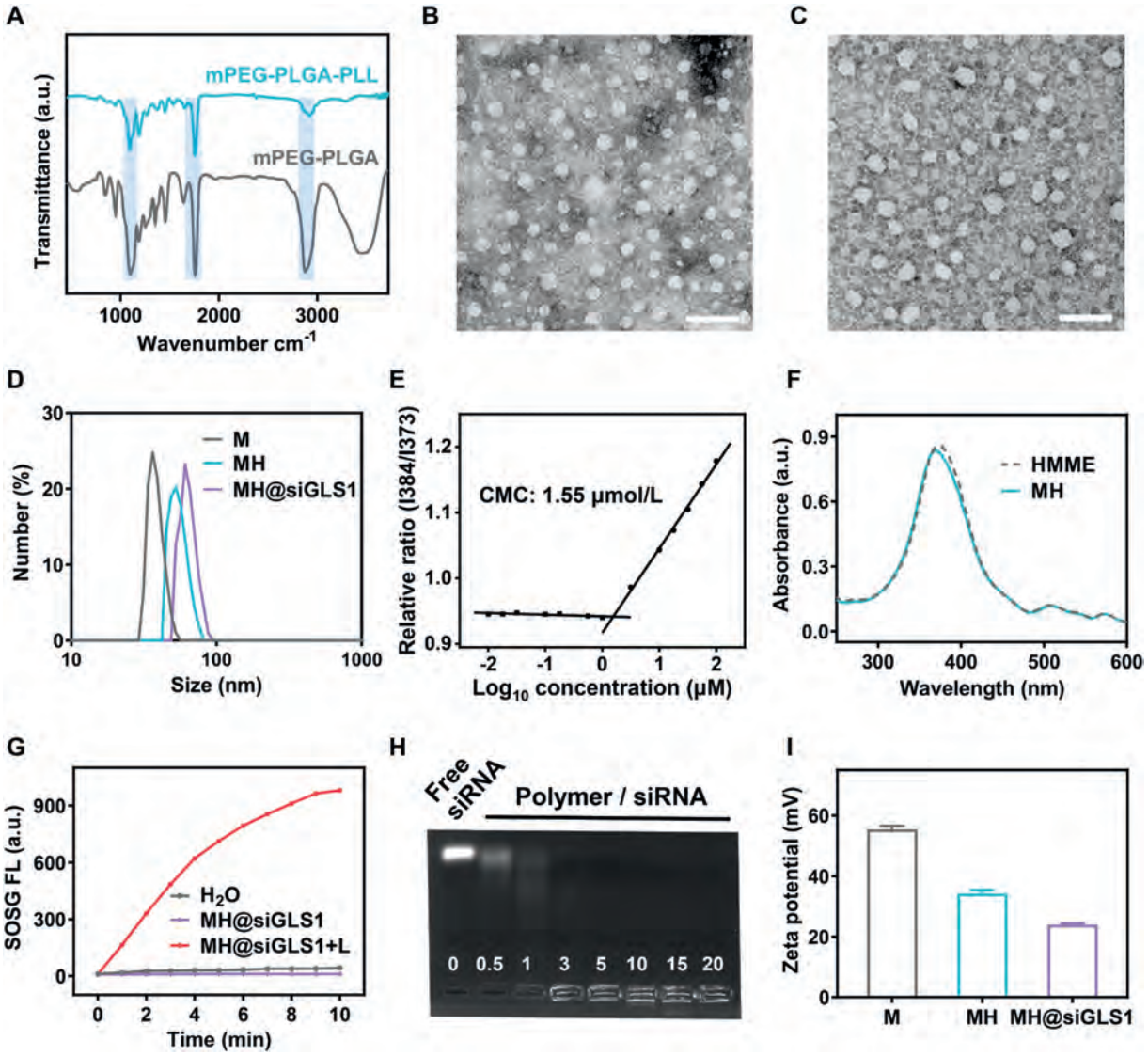

Figure 2 Preparation and characterization of MH@siGLS1. (A) FTIR spectra of the amphiphilic block copolymer mPEG-PLGA-PLL and mPEG-PLGA. (B and C) TEM images of MH (B) and MH@siGLS1 (C). Scale bars = 100 nm. (D) The hydrodynamic particle sizes of M, MH and MH@siGLS1 determined by DLS. (E) The CMC of MH@siGLS1 determined by fluorescence spectra of probe pyrene. (F) UV−vis absorption spectra of free HMME and MH. (G) Time-dependent fluorescence intensity of oxidized SOSG in different groups treated with or without irradiation by a 658 nm laser (100 mW/cm^2). "L" means laser irradiation. (H) Agarose gel electrophoresis assay for siRNA binding affinity of MH micelleplexes at different *N/P* ratios. (I) Zeta potential of M, MH and MH@siGLS1. Data are presented as mean ± SD (n = 5).

diameter of 72.42 ± 6.46 nm determined by dynamic light scattering (DLS). The encapsulation of HMME or siGLS1 could evidently increase the nanoparticle sizes of the micelleplexes (Fig. 2D). And the hydrodynamic diameters of MH@siGLS1 micelleplexes remained stable in 10% serum-contained Dulbecco's Modified Eagle Medium within three days (Supporting Information Fig. S4). The low critical micelle concentration (CMC) of MH@siGLS1 (1.55 μmol/L) (Fig. 2E) further indicated the high stability of the fabricated micelleplexes.

The specific ultraviolet−visible (UV−Vis) adsorption peak of MH at 372 nm suggested the successful encapsulation of HMME in MH micelles (Fig. 2F). Subsequently, the $^1O_2$ generation capability of MH@siGLS1 was evaluated employing the fluorescence probe Singlet Oxygen Sensor Green (SOSG). As shown in Fig. 2G, MH@siGLS1 micelleplexes treated with laser irradiation exhibited a rapid increase in fluorescence intensity in a short time than that without irradiation, demonstrating the sensitive irradiation-dependent $^1O_2$ production capability of MH@siGLS1. To further evaluate the siRNA binding affinity of MH micelleplexes, gel retardation assays were carried out. The cationic polymer mPEG-PLGA-PLL could completely condense siRNA by electrostatic force when the MH-to-siRNA N/P ratio exceeded 3 (Fig. 2H), and the co-incubation of siRNA micelleplexes with 10% serum didn't cause obvious degradation of siRNA (Supporting Information Fig. S5), indicating the stable structure of MH@siGLS1 micelleplexes. The zeta potential of MH after encapsulating HMME (34.24 ± 1.23 mV) and MH@siGLS1 after binding siGLS1 (23.99 ± 0.40 mV) decreased evidently compared to blank M micelles (55.43 ± 1.18 mV), confirming the successful fabrication of stable MH@siGLS1 micelleplexes (Fig. 2I).

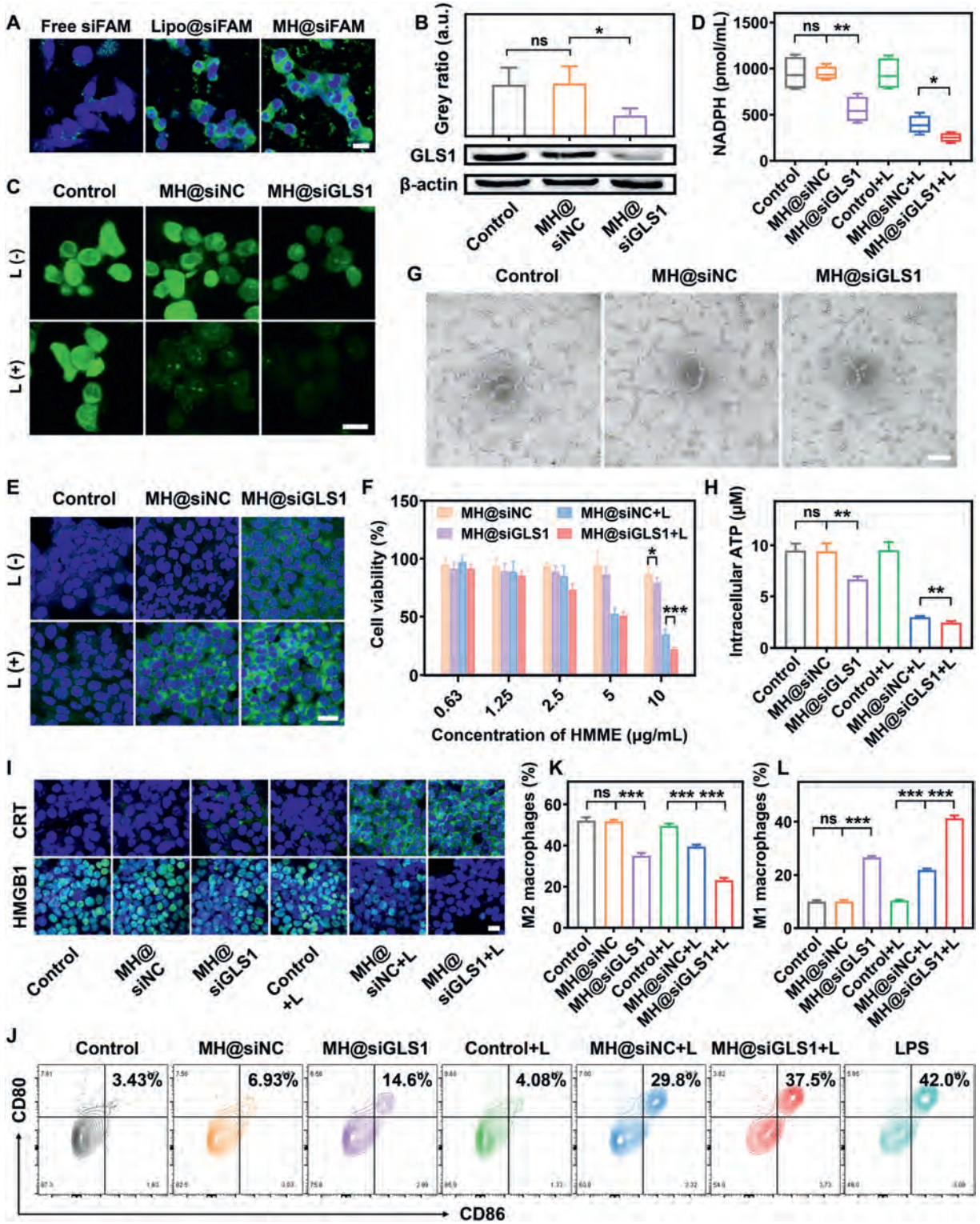

Figure 3 *In vitro* amplified oxidative stress and anti-angiogenesis for enhanced photo-immunotherapy. (A) CLSM examination of the transfection of free siFAM, Lipo@siFAM, and MH@siFAM after 6 h incubation with MC38 cells. DAPI, blue; FAM-labeled siRNA (siFAM), green. Scale bar = 20 μm. (B) Western blotting analysis of GLS1 expressions in MC38 cells after transfection for 48 h with MH@siNC or MH@siGLS1 (the untreated MC38 cells were set as control). Data are presented as mean ± SD (n = 3). (C) CLSM examination of intracellular GSH (green) in MC38 cells with different treatments. Scale bar = 20 μm. (D) Quantitative analysis of NADPH levels in MC38 cells with different treatments. Data are presented as mean ± SD (n = 4). (E) CLSM examination of intracellular ROS generation in MC38 cells with different treatments. Scale bar = 20 μm. (F) MC38 cell viability after 48 h incubation with different treatments. Data are presented as mean ± SD (n = 5). (G) The tube formation of MAEC cells after 4 h incubation with different treatments. Scale bar = 200 μm. (H) Quantitative analysis of intracellular ATP

3.2. *In vitro enhanced oxidative stress, GLS1 silencing and anti-angiogenesis*

Before carrying out cellular experiments, the cellular uptake characteristic of MH@siGLS1 was initially explored based on the intrinsic fluorescence of HMME. As shown in Supporting Information Fig. S6, MH@siGLS1 was efficiently internalized within MC38 cells in a time-dependent manner, and significantly more fluorescence was observed at 6 h compared to that of free HMME, which exhibited almost no cellular engulfment. Large-scale cellular uptake led to efficient FAM-labelled siRNA (siFAM) transfection. As shown in Fig. 3A and Supporting Information Fig. S7, positively charged MH@siFAM exhibited superior transfection efficiency compared to the commercial transfection reagent Lipofectamine 2000, and successfully achieved endo- and lysosomal escape to release siRNA (Supporting Information Fig. S8). Afterward, the GLS1 knockdown efficiency of MH@siGLS1 in tumor cells was analyzed using western blotting (Fig. 3B). MC38 cells without any treatments (Control) or treated with MH@siNC (scrambled control siRNA) showed high GLS1 levels, while MH@siGLS1 significantly suppressed GLS1 expression, verifying the superior GLS1 inhibitory efficiency of the fabricated micelleplexes.

The antioxidant defense systems are usually activated in tumor cells to resist excessive ROS damage by overexpressing GSH, a tripeptide (Glu-Cys-Gly) whose synthesis process is rate-limited by Gln input[4]. As the critical enzyme in glutaminolysis, GLS1 could catalyze Gln towards Glu to provide raw substrate for GSH synthesis[41]. In addition, the generated Gln-derived metabolites are also essential ingredients for malate dehydrogenase, which is important for NADPH generation to maintain the reduced state of GSH[42]. It is reasonable to deduce that the downregulation of GLS1 could break the redox equilibrium state of tumor cells by hampering GSH generation and NADPH production. To prove our assumption, the intracellular GSH level was first investigated in MC38 cells using fluorescent probe ThiolTracker Violet (Fig. 3C and Supporting Information Fig. S9). In contrast to the Control and MH@siNC group, the GLS1 silencing group (MH@siGLS1) exhibited evident GSH depletion capability, indicating that restraining glutaminolysis *via* downregulating GLS1 could disturb GSH synthesis. Among all the groups, MH@siGLS1+L showed the lowest GSH level, which was ascribed to the HMME-mediated intracellular oxidative stress amplification upon laser irradiation, and the generated ROS-mediated GSH consumption to some extent. Subsequently, the intracellular NADPH concentration was further analyzed (Fig. 3D). Same as the GSH detection result, the siGLS1-contained groups exhibited evidently decreased NADPH levels compared to the corresponding siNC-contained groups, demonstrating that GLS1-downregulating could effectively suppress the antioxidant response of tumor cells. The straightforward oxidative effect of MH@siGLS1 was next evaluated using confocal laser scanning microscopy (CLSM) and flow cytometry to visualize the ROS generation. It could be observed that the MH@siGLS1+L group showed the highest ROS production as a consequence of GLS1-downregulating-resulted GSH and NADPH depletion, and HMME-induced $^1O_2$ generation (Fig. 3E, Supporting Information Figs. S10 and S11).

Based on the remarkable oxidative stress caused by MH@siGLS1 under laser irradiation, the cell viabilities of different treatments against MC38 cells were further investigated using the cell counting kit-8 (CCK-8) method. Compared to the Control and MH@siNC groups, the cell viability decreased slightly when treated with MH@siGLS1 (Fig. 3F), supporting the moderate oxidative damage induced by the disruption of the cellular redox equilibrium state (Fig. 3C and D). Comparatively, the HMME-containing groups exhibited prominent phototoxicity upon laser irradiation in an HMME dose-dependent manner. Apart from playing a key role in tumor cell survival, glutaminolysis has also been reported to be closely associated with angiogenesis by participating in the TCA cycle anaplerosis to provide abundant TCA intermediates for macromolecule production of ECs[35]. Thereupon, the anti-angiogenesis *via* hampering glutaminolysis was subsequently investigated in mice aortic endothelial cells (MAEC) utilizing tube formation assay (Fig. 3G and Supporting Information Fig. S12) and transwell cell migration assay (Supporting Information Fig. S13). The results revealed that less tubule formation and cell migration were observed in the MH@siGLS1 group compared to Control and MH@siNC groups, indicating the superb anti-angiogenesis efficiency by inhibiting GLS1 expression to interfere with glutaminolysis within ECs.

3.3. *In vitro immune activation*

It is well-known that PDT is available to trigger immunogenic cell death (ICD), which relies on the released tumor antigens and danger-associated molecular patterns (DAMPs) to perform adaptive antitumor immune responses. To evaluate the ICD induction effect of MH@siGLS1, the typical DAMPs including secreted adenosine triphosphate (ATP), surface-exposed calreticulin (CRT), and released high mobility group box 1 (HMGB1) were initially detected in MC38 cells. As shown in Fig. 3H and I, and Supporting Information Figs. S14 and S15, the MH@siGLS1 group had slight ATP secretion, CRT exposure, and HMGB1 release compared to the Control and MH@siNC groups, indicating that the disruption of cellular redox equilibrium state contributed to the ICD induction to a certain extent. It could be conspicuously observed that the MH@siNC + L group significantly induced DAMPs release, and the GSH and NADPH depletion-promoted PDT oxidative damage further remarkably enhanced the release levels of DAMPs in the MH@siGLS1+L group, suggesting that the degree of ICD was in proportion to ROS accumulation.

The extent of aroused adaptive immune responses was subsequently investigated by measuring DC maturation. Briefly, MC38 cells pretreated with different formulations were incubated with bone marrow-derived DC (BMDCs) for 48 h, then the percentage of matured DC (mDC) was characterized using flow cytometry (Fig. 3J and Supporting Information Fig. S16). Consistent with the results of DAMPs detection, the mDC percentage of the MH@siGLS1 group in the absence of laser

concentration in MC38 cells with different treatments. Data are presented as mean ± SD ($n = 3$). (I) CLSM examination of CRT exposure and HMGB1 release of MC38 cells with different treatments. Scale bar = 20 μm. (J) Flow cytometry examination of *in vitro* DC maturation ($CD80^+CD86^+$, gated on $CD11c^+$) after incubation with MC38 cells in different groups. (K and L) Flow cytometry examination of M2 macrophages ($CD11b^+F4/80^+CD206^+$) (K) and M1 macrophages ($CD11b^+F4/80^+CD86^+$) (L) after different treatments. Data are presented as mean ± SD ($n = 3$). "L" means laser irradiation. *$P < 0.05$, **$P < 0.01$, ***$P < 0.001$. ns, not significant.

irradiation increased slightly compared to the Control and MH@siNC groups, while both the MH@siNC + L and MH@siGLS1+L groups displayed much higher mDC levels compared to their corresponding non-irradiation groups, further confirming that the adaptative antitumor immune responses were intensified with the ROS amplification within tumor cells.

As the main infiltrated immune cells in TME, TAMs possess two typical phenotypes, *i.e.*, anti-tumoral M1 macrophages and pro-tumoral M2 macrophages. It's worth noting that the immunosuppressive M2 macrophages have been reported to rely more on glutaminolysis than M1 macrophages[41]. As a consequence, Gln deprivation by downregulating the expression of GLS1, an essential enzyme of glutaminolysis, is theoretically available to repolarize M2 macrophages into the M1 phenotype. To verify this assumption, *in vitro* M2 macrophages repolarization experiment was carried out using flow cytometry. As shown in Fig. 3K, L, and Supporting Information Fig. S17, the siGLS1-contained groups obviously exhibited lower percentages of M2 macrophages and higher percentages of M1 macrophages compared to their corresponding siNC-contained groups, demonstrating that the inhibition of glutaminolysis could effectively repolarize the M2 macrophages towards M1 phenotype. Interestingly, the PDT groups (MH@siNC + L and MH@siGLS1+L) displayed much higher repolarization efficiency than their corresponding non-PDT groups, which could be ascribed to that elevated ROS favored the switch of M2 phenotype towards M1 by acting as immune response initiator and enhancer[37].

3.4. Biosafety and in vivo biodistribution

Before carrying out *in vivo* antitumor experiments, *in vitro* and *in vivo* biosafety studies of MH@siGLS1 were initially investigated. As shown in Supporting Information Fig. S18, MH@siNC and MH@siGLS1 exhibited low cytotoxicity against normal cells (MAEC and NIH 3T3), supporting their good biosafety. Afterward, the *in vitro* cellular uptake was performed to evaluate the phagocytosis amount of MH@siGLS1 by selecting three types of different cells, including MC38, RAW 264.7, and MAEC, to represent tumor cells, TAMs, and vascular endothelial cells in TME respectively (Supporting Information Fig. S19). The significantly higher cellular uptake of MH@siGLS1 was observed in MC38 cells, followed by RAW 264.7 and MAEC. Such a phenomenon could be ascribed to that tumor cells and TAMs are phagocytic cells that possess higher engulfment capabilities than other cells. Especially, the extremely high nutritional requirements of tumor cells determined their prominent cellular uptake, which also ensured the maximum damage to tumor cells when applying laser irradiation. In addition, the low hemolysis rates of MH@siGLS1 proved the safety of intravenous administration (Supporting Information Fig. S20), which indicated the potential for further biomedical applications. According to the results of biochemistry and complete blood panel analysis (Supporting Information Figs. S21 and S22), no obvious differences in the liver (ALT and AST) and kidney (BUN and CREA) function indicators, and complete blood count were observed among the control group and treatment groups, further demonstrating the low short-term toxicity and low long-term toxicity of MH@siGLS1.

In order to guarantee the effectuality of MH@siGLS1 for further *in vivo* antitumor therapy, the biodistribution characteristic was subsequently evaluated on the MC38 tumor-bearing C57BL/6 mice by tracking the intrinsic fluorescence of HMME after intravenously injected MH@siGLS1 or free HMME at an identical HMME dose of 5 mg/kg (Fig. 4A). Compared to free HMME group, the mice treated with MH@siGLS1 exhibited remarkably increased fluorescence accumulation in tumor regions over time, and reached a maximum value at 24 h post-injection (Fig. 4B). The consequential slow decay of fluorescence implied the body degradation and excretion of MH@siGLS1. The subsequent *ex vivo* fluorescence images of the collected tumor and major organs indicated that MH@siGLS1 possessed excellent retention capability in tumor tissue even after 48 h post-injection (Fig. 4C and D), which was the prerequisite for antitumor therapeutic efficacy. Comparatively, obviously weaker fluorescence of the free HMME group was detected in tumor tissue compared to the MH@siGLS1 group.

3.5. In vivo vascular normalization and ICD induction

Encouraged by the superb tumor accumulation ability, we further investigated the vascular normalization and ICD induction effect of MH@siGLS1 in the unilateral MC38 tumor-bearing C57BL/6 mice model (Fig. 5A). In brief, mice were randomly divided into 6 groups ($n = 5$ per group) when the tumor volumes reached 100 mm^3 and intravenously injected with either PBS, MH@siNC or MH@siGLS1 on Days 0, 2, 4, respectively. Three irradiated groups (Control + L, MH@siNC + L, and MH@siGLS1+L) received 5 min of laser irradiation (658 nm, 300 mW/cm^2) 24 h post-injection. *In vitro* studies have demonstrated that inhibiting glutaminolysis by downregulating GLS1 expression could effectively hamper the endothelial cell tube formation and migration (Fig. 3G, Figs. S12 and S13). In order to verify whether glutaminolysis inhibition also contributed to the *in vivo* vascular system, the tumor tissues harvested at the treatment endpoint were sliced for further immunostaining. As indicated in Fig. 5B, the vessel marker CD31 (red) in siGLS1-contained groups (MH@siGLS1 and MH@siGLS1+L) were significantly decreased and more ordered compared to the other four groups, proving that inhibiting glutaminolysis could beneficially reduce vessel density and convert the chaotic tumor vessels to a systematic state. In addition, conspicuously elevated colocalization levels of the pericyte marker α-smooth muscle actin (α-SMA) (green) with CD31 in the two siGLS1-contained groups further verified the increased vascular maturation, which is a significant sign for vascular normalization (Supporting Information Fig. S23E).

In order to meet the requirement of nutrients for malignant expansion, solid tumors usually tend to enable the rapid formation of the pathological tumor vessels *via* upregulating angiogenesis factors, including hypoxia-inducible factor-1α (HIF-1α) and vascular endothelial growth factor (VEGF), which contributed to the construction of hypoxic TME that further hampered the deep infiltration and therapeutic effect of drugs and immune cells. To evaluate whether vascular normalization alleviated tumor hypoxia, the HIF-1α and VEGF levels in tumor regions were further investigated *via* immunofluorescence staining. As indicated in Fig. 5C, Supporting Information Fig. S23A, S23B and S23F, both HIF-1α and VEGF levels of the siGLS1-contained groups were obviously lower than that of the other groups, proving that the glutaminolysis intervention of ECs by downregulating GLS1 expressions in tumor regions (Fig. 5D and Supporting Information Fig. S23C) benefited the hypoxia alleviation by achieving vascular normalization.

Furthermore, the CRT expressions of tumor tissues were examined using immunofluorescence staining to investigate the

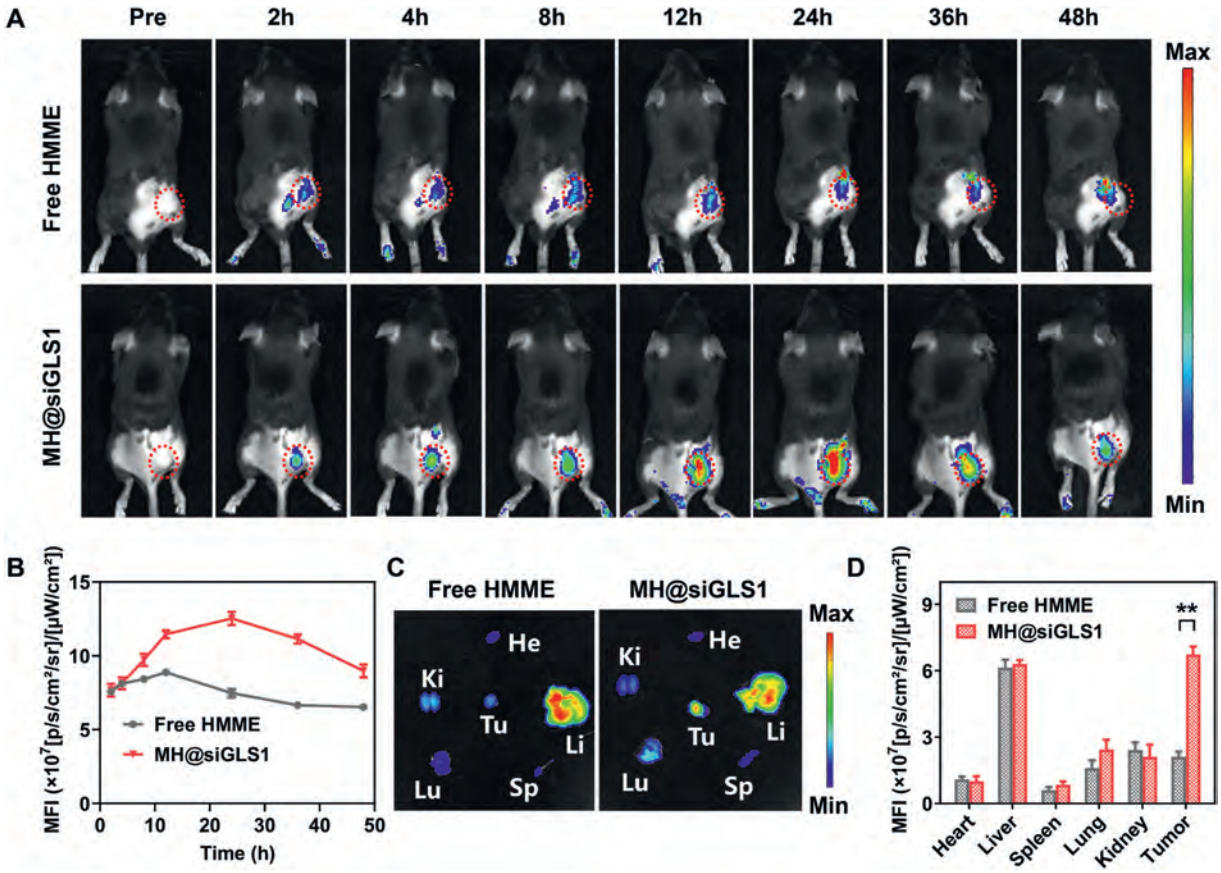

Figure 4 *In vivo* biodistribution. (A and B) *In vivo* fluorescence images of MC38 tumor-bearing mice at different time points after intravenous injection of free HMME or MH@siGLS1 (A) and the corresponding quantification of mean fluorescence intensity (MFI) values in tumor regions (B). Data are presented as mean ± SD ($n = 3$). (C and D) *Ex vivo* fluorescence images of major organs and tumor tissues harvested at 48 h post-injection (C) and the corresponding quantification of MFI values (D). Data are presented as mean ± SD ($n = 3$). "L" means laser irradiation. $^*P < 0.05$, $^{**}P < 0.01$, $^{***}P < 0.001$. ns, not significant.

ICD induction effect. As shown in Fig. 5E and Supporting Information Fig. S23D, MH@siGLS1+L exhibited the maximum CRT exposure due to the remarkable amplified oxidative stress by GLS1-downregulation promoted PDT efficacy.

3.6. *Antitumor therapeutic efficiency*

The antitumor therapeutic efficiency of MH@siGLS1 in the unilateral MC38 tumor-bearing C57BL/6 mice model was investigated meanwhile. As shown in Fig. 6A−C, Control, Control + L, and MH@siNC groups exhibited almost no tumor growth inhibitory effect, demonstrating that single laser irradiation or MH@siNC injection could not perform valid antitumor efficacy. As anticipated, the MH@siGLS1 group showed slightly better antitumor effect compared to the MH@siNC group, which was ascribed to the short supply of nutrients caused by the inhibition of the TCA cycle *via* hampering glutaminolysis, and the accompanying damage of redox equilibrium state in tumor cells through suppressing GSH synthesis and NADPH production. Comparatively, two PDT groups (MH@siNC + L and MH@siGLS1+L) exhibited superb tumor inhibitory efficacy owing to their straightforward oxidative effect by generating abundant ROS. It is noteworthy that the tumors of MH@siGLS1+L were almost completely suppressed, which was beneficial from the nutrient deficit and the consequential amplified oxidative stress *via* inhibiting glutaminolysis. Hematoxylin and eosin (H&E) staining and terminal deoxynucleotidyl transferase dUTP nick-end labeling (TUNEL) staining of tumor tissues further revealed that the tumor cell apoptosis and necrosis were in proportion to the generated ROS levels (Fig. 6D and E). Additionally, no obvious body-weight loss (Supporting Information Fig. S24), nor pathological damage according to H&E staining of major organs (heart, liver, spleen, lung, and kidney) (Supporting Information Fig. S25) was observed, demonstrating the acceptable biosafety of the applied treatments.

3.7. *Abscopal effect and immune activation*

Given the inspiration of the excellent antitumor efficacy, the immune activation was further investigated in a bilateral MC38 tumor-bearing C57BL/6 mice model (Fig. 7A). Mice were randomly divided into 6 groups ($n = 5$ per group) when the tumor volumes reached 100 mm^3 and intravenously injected with either PBS, MH@siNC or MH@siGLS1 (three groups received *i.v.* injections only, and the other three irradiated groups received laser irradiation 24 h post-injection). Consistent with the result of tumor growth in the unilateral MC38 tumor-bearing C57BL/6 mice model, both the primary and abscopal tumors in the

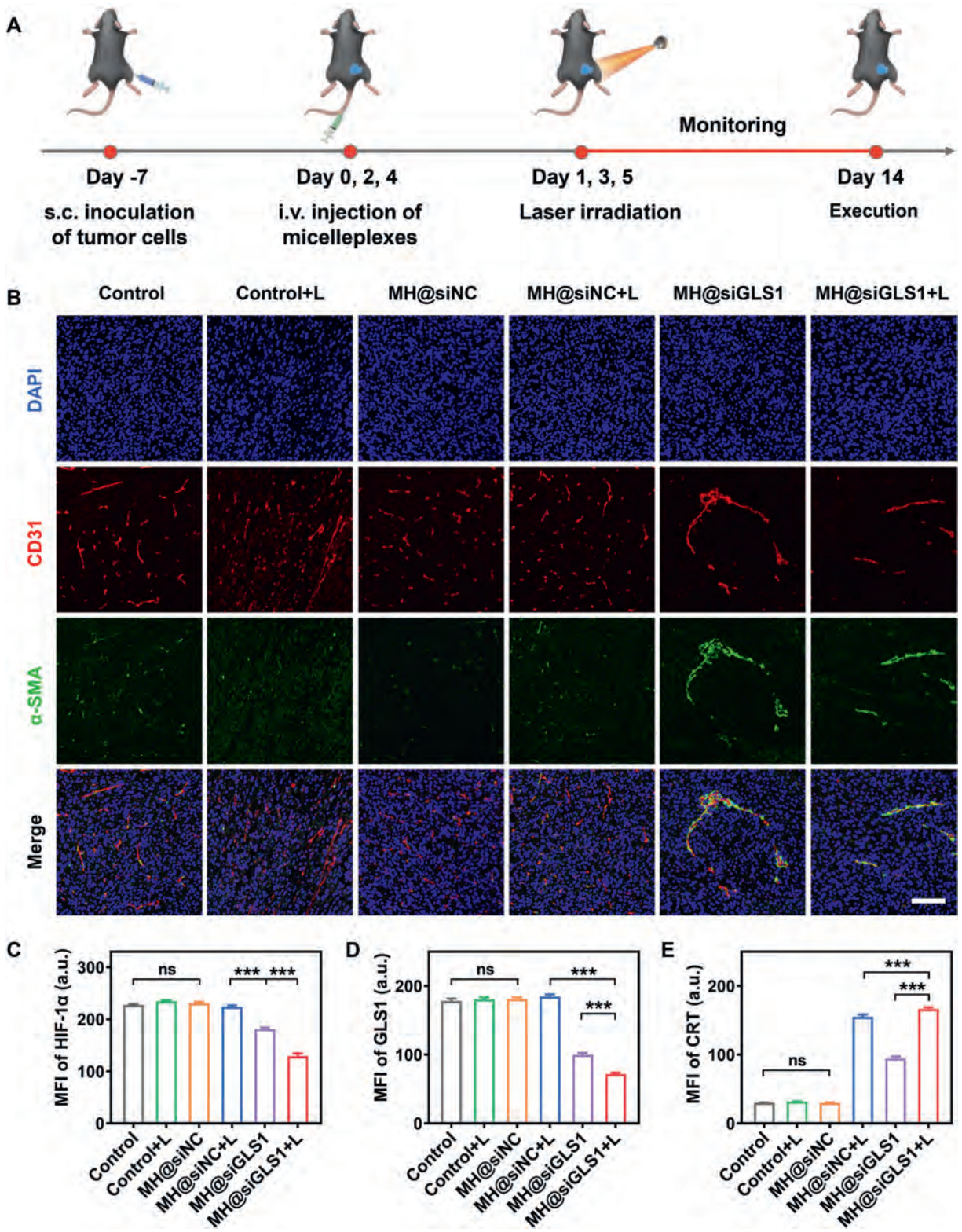

Figure 5 Vascular normalization and ICD induction. (A) Treatment schedule for *in vivo* antitumor efficacy in the unilateral MC38 tumor-bearing mice model. *s.c.*, subcutaneous. i.v., intravenous. (B) Representative immunofluorescent images of vessel density (CD31, red) and pericyte coverage (α-SMA, green) on the endothelium of tumor tissues in different groups. Scale bar = 100 μm. (C–E) The quantitative fluorescence analysis of HIF-1α (C), GLS1 (D), and CRT (E) levels in tumor tissues. Data are presented as mean ± SD ($n = 5$). "L" means laser irradiation. $^{*}P < 0.05$, $^{**}P < 0.01$, $^{***}P < 0.001$. ns, not significant.

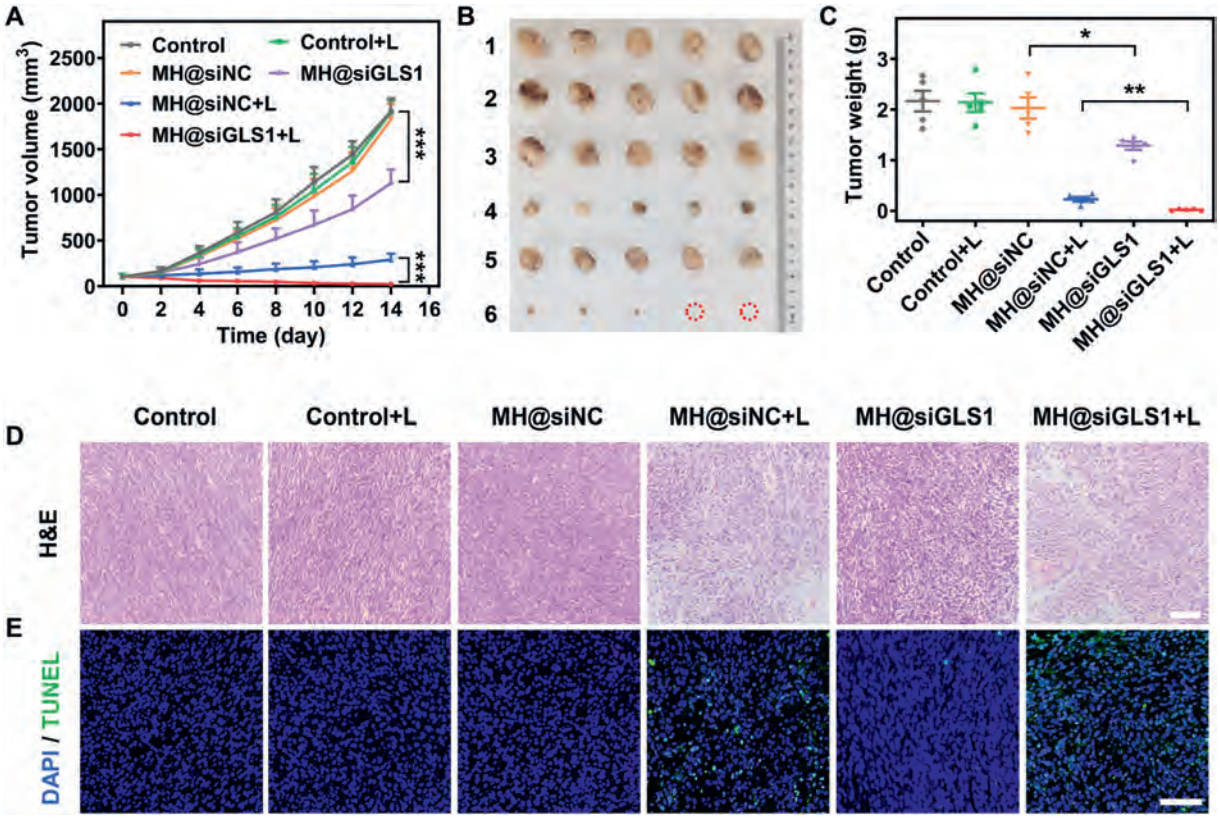

Figure 6 Antitumor efficacy. (A) Tumor growth curves of the unilateral MC38 tumor-bearing mice. Data are presented as mean ± SD ($n = 5$). (B and C) Photograph (1: Control; 2: Control + L; 3: MH@siNC; 4: MH@siNC + L; 5: MH@siGLS1; 6: MH@siGLS1+L) (B) and the corresponding weights (C) of the resected tumors in different groups at the end of treatment. (D and E) H&E (D) and TUNEL staining (E) images of the tumor tissues in different groups. Scale bars = 100 μm "L" means laser irradiation. *$P < 0.05$, **$P < 0.01$, ***$P < 0.001$. ns, not significant.

MH@siGLS1+L group exhibited the most superb tumor inhibitory efficiency, followed by MH@siNC + L group (Fig. 7B and C), demonstrating the successful stimulation of systemic immune responses. It is worth noting that single MH@siGLS1 could also suppress the abscopal tumor growth to a certain extent, which might be predominantly beneficial from the drug accumulation in the abscopal tumor region and the subsequent glutaminolysis inhibition effect. This indicated that the inhibition of abscopal tumors depended on the synergistic function of the intrinsic drug therapeutical effect and the immune responses initiated by PDT-boosted ICD. No significant body-weight loss was observed in the mice during the 14-day treatment (Fig. 7D).

The antitumor immune responses were further investigated by analyzing tumor-draining lymph nodes (TDLNs)-resident DCs, and tumor tissues-infiltrated T cells, Treg cells, and TAMs using flow cytometry. DCs acted as the bridge linking innate immunity and adaptive immunity, and the maturation rates of DCs were crucial for initiating antitumor immune responses. It could be observed that MH@siNC exhibited almost no DC maturation compared to the Control and Control + L groups since no drug therapeutic effect or PDT therapy functioned. While MH@siGLS1 caused moderate DC maturation due to the inadequate ICD induction by disrupting the redox equilibrium of tumor cells *via* downregulating GLS1 expression merely (Fig. 7E and Supporting Information Fig. S26). Evidently increased DC maturation rates were observed in the laser irradiation groups (MH@siNC + L and MH@siGLS1+L), emphasizing that PDT was the main cause of inducing sufficient ICD. It is noteworthy that the siGLS1-amplified oxidative damage by inhibiting GSH and NADPH production in the MH@siGLS1+L group was conducive to higher DC maturation efficacy than the MH@siNC + L group.

As the main antitumor immune system, the tumor-specific adaptive immunity could be subsequently activated after presenting the processed antigens to T lymphocytes by mature DCs. In order to better evaluate the adaptive immune responses, the tumor-infiltrated $CD4^+$ helper T cells (Fig. 7F and Supporting Information Fig. S27) and $CD8^+$ cytotoxic T cells (Fig. 7G and Supporting Information Fig. S28) in primary tumors were further detected. Concordant with the results of mature DCs, the MH@siGLS1+L group exhibited the highest $CD4^+$ T and $CD8^+$ T cell infiltration rates (33.5% and 33.6% respectively), confirming the extraordinary antitumor immune responses mediated by the united effect of redox equilibrium disruption, PDT-induced oxidative damage, and tumor vascular normalization-boosted immune cells infiltration. Conversely, the trend of the immunosuppressive Treg cells population was opposite to that of $CD4^+$ T and $CD8^+$ T cells (Fig. 7H and Supporting Information Fig. S29).

It has been proved that the glutaminolysis inhibition of ECs contributed to the tumor vascular normalization (Fig. 5B), which favored the hypoxia alleviation of tumor tissues (Fig. 5C,

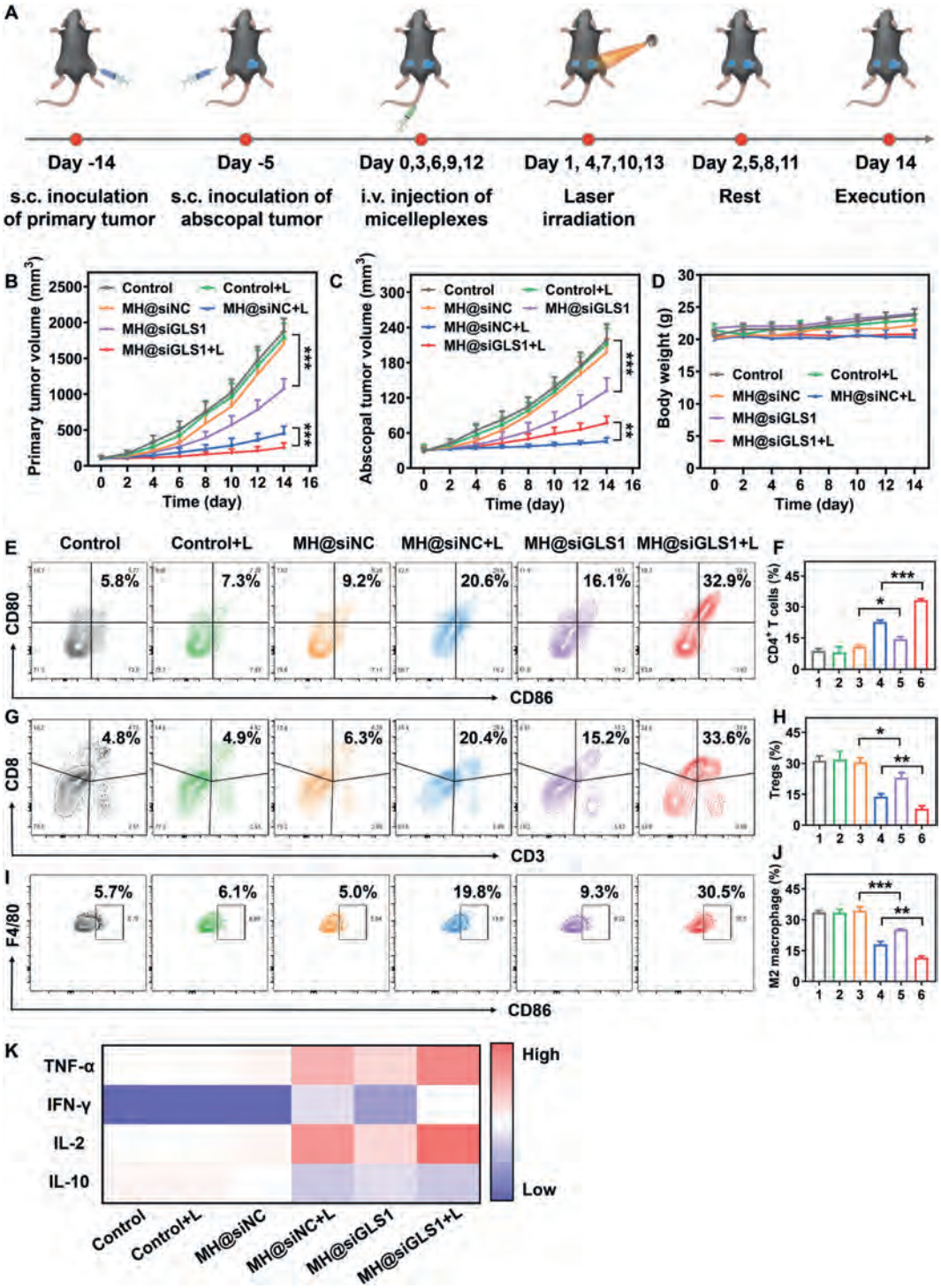

Figure 7 *In vivo* immune activation. (A) Treatment schedule for MH@siGLS1-medaited abscopal effect in the bilateral MC38 tumor-bearing mice model. s.c., subcutaneous. i.v., intravenous. (B and C) Primary (B) and abscopal (C) tumor growth curves of the bilateral MC38 tumor-bearing mice during the experimental period. Data are presented as mean ± SD ($n = 5$). (D) Body weights of the bilateral MC38 tumor-bearing mice during the experimental period. Data are presented as mean ± SD ($n = 5$). (E) Flow cytometry examination of mature DCs ($CD80^+CD86^+$, gated on $CD11c^+$) in the TDLNs of the bilateral MC38 tumor-bearing mice post-treatments. (F) Quantification of intratumorally infiltrated $CD4^+$ T cells post-treatments (1: Control; 2: Control + L; 3: MH@siNC; 4: MH@siNC + L; 5. MH@siGLS1; 6: MH@siGLS1+L). Data are presented as mean ± SD ($n = 3$). (G) Flow cytometry examination of intratumorally infiltrated $CD8^+$ T cells ($CD3^+CD8^+$) post-treatments. (H) Quantification of intratumorally infiltrated Treg cells post-treatments. Data are presented as mean ± SD ($n = 3$). (I) Flow cytometry examination of intratumorally infiltrated M1 macrophages ($F4/80^+CD86^+$, gated on $CD11b^+F4/80^+$) post-treatments. (J) Quantification of intratumorally infiltrated M2 macrophages post-treatments. Data are presented as mean ± SD ($n = 3$). (K) The heatmaps of the content of TNF-α, IFN-γ, IL-2 and IL-10 within the tumor tissues post-treatments. Data are presented as mean ± SD ($n = 3$). "L" means laser irradiation. $^*P < 0.05$, $^{**}P < 0.01$, $^{***}P < 0.001$. ns, not significant.

Supporting Information Fig. S23A, S23B, S23F). As the most abundant tumor-resident innate immune cells, the phenotypes of TAMs are greatly affected by the hypoxia levels. The hypoxic TME has been reported to promote the anti-tumoral M1 phenotype towards the pro-tumoral M2 phenotype, which suppresses immune system activation by secreting anti-inflammatory cytokines including IL-4 and upregulating immunosuppressive molecules such as signal regulatory protein α (SIRPα) to help tumor cells achieve immune escape. Specifically, inhibiting glutaminolysis of TAMs could support the repolarization of M2 macrophages towards the M1 phenotype due to the higher Gln-dependence of M2 macrophages than M1 (Fig. 3K and L)[41]. Therefore, the TAMs including M1 macrophages (Fig. 7I and Supporting Information Fig. S30) and M2 macrophages (Fig. 7J and Supporting Information Fig. S31) infiltrated in tumor tissues were next analyzed. As the results indicated, the siGLS1-contained groups obviously possessed higher TAMs repolarization rates than their corresponding siNC-contained groups, which might be ascribed to the synergistic effect of vascular normalization-mediated hypoxia alleviation and Gln-dependent destruction in M2 macrophages *via* downregulating GLS1 expressions. It's worth noting that MH@siNC + L displayed higher TAMs repolarization rates than MH@siGLS1 due to the fact that elevated ROS by PDT promoted TAMs repolarization from M2 phenotype towards M1 by acting as immune response initiator and enhancer, indicating that the ROS level also played a key role in TAMs repolarization.

Inspired by the encouraging findings of antitumor immune responses, the content of released cytokines within the tumor tissues was next measured using enzyme-linked immunosorbent assay (ELISA) to further evaluate the immune activation degree (Fig. 7K). The content of immune-stimulating cytokines including TNF-α, IFN-γ, and IL-2 was appreciably increased in the PDT groups, while the immunosuppressive cytokine IL-10 was remarkably decreased, indicating the sufficient induction of ICD and successful activation of antitumor immunity.

4. Conclusions

As an extremely heterogeneous pathological "organ", tumors consist of cells with different metabolic characteristics that are hijacked to serve the rapid expansion of tumor cells. To satisfy the high demand for energy and biomass synthesis, tumor cells strengthen glutaminolysis to fuel the TCA cycle and build antioxidant systems. In order to obtain more nutrients, ECs are also expropriated to establish tumor vessels by accelerating glutaminolysis, ultimately promoting the formation of immunosuppressive TME featured with hypoxia and low immune effector cell infiltration. By contrast, the population of another immunosuppressive M2 macrophages undergoing Gln metabolic switch is increased to hamper antitumor immunity.

Herein, we reported a photo-immunometabolic strategy by re-engineering glutaminolysis of tumor-resident cell types to reverse the immunosuppressive TME for efficient antitumor immunity. By interrupting the TCA cycle, MH@siGLS1-mediated glutaminolysis inhibition could achieve tumor cell starvation and destroy the cellular redox equilibrium, thus benefiting the oxidative damage-dependent PDT that simultaneously triggered adaptive antitumor immunity *via* inducing ICD. Meanwhile, hampering glutaminolysis in tumor ECs and TAMs could respectively lead to the tumor vascular normalization and repolarization of M2 macrophages towards M1 phenotype, thus promoting the reversion of immunosuppressive TME to amplify the antitumor photo-immunotherapy and block tumor cell escape.

Acknowledgments

The authors gratefully acknowledge the support of this research by National Key Research and Development Program of China (2023YFD1800105), National Natural Science Foundation of China (32322043, 32171313, and 82272154), Tianjin Science Fund for Distinguished Young Scholars (22JCJQJC00120, China), Shenzhen Science and Technology Program (RCYX20210706092104033, and JCYJ20210324124402006, China), the Fundamental Research Funds for the Central Universities (2021-RC310-005, China), Science and Technology Program of Tianjin City (the Basic Research Cooperation Special Foundation of Beijing-Tianjin-Hebei Region, 22JCZXJC00060, China), Chinese Academy of Medical Sciences Innovation Fund for Medical Sciences (2024-I2M-TS-028, 2021-I2M-5-012, 2021-I2M-1-058, and 2022-I2M-2-003, China).

Author contributions

Yunfei Yi: Writing − original draft, Methodology, Investigation, Formal analysis, Data curation, Conceptualization. Zhangwen Peng: Writing − original draft, Validation, Software, Methodology, Investigation, Data curation. Yuanqi Liu: Methodology, Investigation, Formal analysis. Huisong Hao: Visualization, Validation, Methodology, Investigation. Liu Yu: Methodology, Investigation. Simin Wen: Methodology, Investigation. Shengjie Sun: Methodology, Investigation. Jianlin Shi: Supervision, Funding acquisition. Meiying Wu: Writing − review & editing, Supervision, Project administration, Funding acquisition, Conceptualization. Lin Mei: Writing − review & editing, Supervision, Resources, Project administration, Funding acquisition, Conceptualization.

Conflicts of interest

The authors declare no conflicts of interest.

Appendix A. Supporting information

Supporting information to this article can be found online at https://doi.org/10.1016/j.apsb.2025.02.020.

References

1. Raines LN, Huang SC-C. Is glucose the scapegoat for tumor evasion?. *Cancer Cell* 2021;**39**:907−9.
2. Li C, Wang JC, Wang YG, Gao HL, Wei G, Huang YZ, et al. Recent progress in drug delivery. *Acta Pharm Sin B* 2019;**9**:1145−62.
3. Reinfeld BI, Madden MZ, Wolf MM, Chytil A, Bader JE, Patterson AR, et al. Cell-programmed nutrient partitioning in the tumour microenvironment. *Nature* 2021;**593**:282−8.
4. Altman BJ, Stine ZE, Dang CV. From Krebs to clinic: glutamine metabolism to cancer therapy. *Nat Rev Cancer* 2016;**16**:619−34.
5. Gao MH, Yi JM, Zhu JJ, Minikes AM, Monian P, Thompson CB, et al. Role of mitochondria in ferroptosis. *Mol Cell* 2019;**73**:354−63.e3.
6. Son J, Lyssiotis CA, Ying HQ, Wang XX, Hua S, Ligorio M, et al. Glutamine supports pancreatic cancer growth through a KRAS-regulated metabolic pathway. *Nature* 2013;**496**:101−5.

7. Lin CC, Huang CY, Shi ZQ, Ou MT, Sun SJ, Yu M, et al. Biodegradable calcium sulfide-based nanomodulators for H2S-boosted Ca^{2+}-involved synergistic cascade cancer therapy. *Acta Pharm Sin B* 2022;**12**:4472−85.
8. Botman D, Tigchelaar W, Van Noorden CJ. Determination of phosphate-activated glutaminase activity and its kinetics in mouse tissues using metabolic mapping (quantitative enzyme histochemistry). *J Histochem Cytochem* 2014;**62**:813−26.
9. DeBerardinis RJ, Mancuso A, Daikhin E, Nissim I, Yudkoff M, Wehrli S, et al. Beyond aerobic glycolysis: transformed cells can engage in glutamine metabolism that exceeds the requirement for protein and nucleotide synthesis. *Proc Natl Acad Sci U S A* 2007;**104**:19345−50.
10. Chen T, Zeng WW, Liu YQ, Yu M, Huang CY, Shi ZQ, et al. Cu-doped polypyrrole with multi-catalytic activities for sono-enhanced nanocatalytic tumor therapy. *Small* 2022;**18**:e2202964.
11. Li QQ, Shi ZQ, Zhang F, Zeng WW, Zhu DW, Mei L. Symphony of nanomaterials and immunotherapy based on the cancer−immunity cycle. *Acta Pharm Sin B* 2022;**12**:107−34.
12. Xiao QQ, Li XT, Liu C, Jiang YX, He YL, Zhang WT, et al. Improving cancer immunotherapy *via* co-delivering checkpoint blockade and thrombospondin-1 downregulator. *Acta Pharm Sin B* 2023;**13**:3503−17.
13. Xie YY, Li XT, Wu JY, Zeng HL, Boucetta H, Wang B, et al. CAR-T cells for cancer immunotherapy. *Chin Chem Lett* 2023;**34**:108202.
14. Martin JD, Seano G, Jain RK. Normalizing function of tumor vessels: progress, opportunities, and challenges. *Annu Rev Physiol* 2019;**81**: 505−34.
15. Liu ZG, Wang YF, Huang YH, Kim BYS, Shan H, Wu DP, et al. Tumor vasculatures: a new target for cancer immunotherapy. *Trends Pharmacol Sci* 2019;**40**:613−23.
16. Jain RK. Antiangiogenesis strategies revisited: from starving tumors to alleviating hypoxia. *Cancer Cell* 2014;**26**:605−22.
17. Viallard C, Larrivee B. Tumor angiogenesis and vascular normalization: alternative therapeutic targets. *Angiogenesis* 2017;**20**:409−26.
18. Ramjiawan RR, Griffioen AW, Duda DG. Anti-angiogenesis for cancer revisited: is there a role for combinations with immunotherapy?. *Angiogenesis* 2017;**20**:185−204.
19. Kuczynski EA, Vermeulen PB, Pezzella F, Kerbel RS, Reynolds AR. Vessel co-option in cancer. *Nat Rev Clin Oncol* 2019;**16**:469−93.
20. Jain RK. Normalizing tumor microenvironment to treat cancer: bench to bedside to biomarkers. *J Clin Oncol* 2013;**31**:2205−18.
21. Zhao Y, Ting KK, Coleman P, Qi YF, Chen JB, Vadas M, et al. The tumour vasculature as a target to modulate leucocyte trafficking. *Cancers (Basel)* 2021;**13**:1724.
22. Jain RK. Normalization of tumor vasculature: an emerging concept in antiangiogenic therapy. *Science* 2005;**307**:58−62.
23. Martin JD, Cabral H, Stylianopoulos T, Jain RK. Improving cancer immunotherapy using nanomedicines: progress, opportunities and challenges. *Nat Rev Clin Oncol* 2020;**17**:251−66.
24. Huang YH, Kim BYS, Chan CK, Hahn SM, Weissman IL, Jiang W. Improving immune-vascular crosstalk for cancer immunotherapy. *Nat Rev Immunol* 2018;**18**:195−203.
25. Yi YF, Yu M, Feng C, Hao HS, Zeng WW, Lin CC, et al. Transforming "cold" tumors into "hot" ones *via* tumor-microenvironment-responsive siRNA micelleplexes for enhanced immunotherapy. *Matter* 2022;**5**: 2285−305.
26. Li XR, Sun XD, Carmeliet P. Hallmarks of endothelial cell metabolism in health and disease. *Cell Metab* 2019;**30**:414−33.
27. Chung AS, Ferrara N. Developmental and pathological angiogenesis. *Annu Rev Cell Dev Biol* 2011;**27**:563−84.
28. Chekhonin VP, Shein SA, Korchagina AA, Gurina OI. VEGF in tumor progression and targeted therapy. *Curr Cancer Drug Targets* 2013;**13**: 423−43.
29. Yang YL, Cao YH. The impact of VEGF on cancer metastasis and systemic disease. *Semin Cancer Biol* 2022;**86**:251−61.
30. Gacche RN, Assaraf YG. Redundant angiogenic signaling and tumor drug resistance. *Drug Resist Updates* 2018;**36**:47−76.
31. Wang ZW, Dabrosin C, Yin X, Fuster MM, Arreola A, Rathmell WK, et al. Broad targeting of angiogenesis for cancer prevention and therapy. *Semin Cancer Biol* 2015;**35**:S224−43.
32. Ebos JML, Kerbel RS. Antiangiogenic therapy: impact on invasion, disease progression, and metastasis. *Nat Rev Clin Oncol* 2011;**8**: 210−21.
33. De Bock K, Georgiadou M, Schoors S, Kuchnio A, Wong BW, Cantelmo AR, et al. Role of PFKFB3-driven glycolysis in vessel sprouting. *Cell* 2013;**154**:651−63.
34. Buchwald P. A local glucose-and oxygen concentration-based insulin secretion model for pancreatic islets. *Theor Biol Med Modell* 2011;**8**: 20.
35. Huang HL, Vandekeere S, Kalucka J, Bierhansl L, Zecchin A, Bruning U, et al. Role of glutamine and interlinked asparagine metabolism in vessel formation. *EMBO J* 2017;**36**:2334−52.
36. Jin J, Byun JK, Choi YK, Park KG. Targeting glutamine metabolism as a therapeutic strategy for cancer. *Exp Mol Med* 2023;**55**: 706−15.
37. Zeng WW, Yu M, Chen T, Liu YQ, Yi YF, Huang CY, et al. Polypyrrole nanoenzymes as tumor microenvironment modulators to reprogram macrophage and potentiate immunotherapy. *Adv Sci* 2022; **9**:e2201703.
38. Doedens AL, Stockmann C, Rubinstein MP, Liao D, Zhang N, DeNardo DG, et al. Macrophage expression of hypoxia-inducible factor-1 alpha suppresses T-cell function and promotes tumor progression. *Cancer Res* 2010;**70**:7465−75.
39. Leone RD, Zhao L, Englert JM, Sun IM, Oh MH, Sun IH, et al. Glutamine blockade induces divergent metabolic programs to overcome tumor immune evasion. *Science* 2019;**366**: 1013−21.
40. Liu PF, Yu H, Sun Y, Zhu MJ, Duan YR. A mPEG-PLGA-b-PLL copolymer carrier for adriamycin and siRNA delivery. *Biomaterials* 2012;**33**:4403−12.
41. Mai ZY, Zhong J, Zhang JS, Chen GM, Tang Y, Ma W, et al. Carrier-free immunotherapeutic nano-booster with dual synergistic effects based on glutaminase inhibition combined with photodynamic therapy. *ACS Nano* 2023;**17**:1583−96.
42. Dornier E, Rabas N, Mitchell L, Novo D, Dhayade S, Marco S, et al. Glutaminolysis drives membrane trafficking to promote invasiveness of breast cancer cells. *Nat Commun* 2017;**8**:2255.